SCIENCE CHINA
Physics, Mechanics & Astronomy

•Article•

November 2019 Vol. 62 No. 11: 114711
https://doi.org/10.1007/s11433-019-9398-5

Gusty wind disturbances and large-scale turbulent structures in the neutral atmospheric surface layer

HaiHua Gu[1], GuoHua Wang[1], Wei Zhu[1], and XiaoJing Zheng[2*]

[1] *Key Laboratory of Mechanics on Disaster and Environment in Western China, Lanzhou University, Lanzhou 730000, China;*
[2] *Research Center for Applied Mechanics, School of Mechano-Electronic Engineering, Xidian University, Xi'an 710071, China*

Received January 19, 2019; accepted March 25, 2019; published online April 29, 2019

This study analyzes the contribution of large-scale turbulent structures, including very large-scale and large-scale motions, to the streamwise turbulent kinetic energy and momentum flux in comparison with the contribution of the gusty wind disturbances based on the high-quality data obtained from the field measurements conducted in the near-neutral surface layer. The results of this study denote that the gusty wind disturbances contain only a portion of the energy contained in very large-scale motions and do not contain any of the information contained in large-scale motions. The amount of lost contributions to the streamwise turbulent kinetic energy and momentum flux increases linearly with the friction velocity, eventually becoming 53% and 67%, respectively. This indicates that large-scale turbulent structures (very large-scale motions and large-scale motions) better describe the coherent structures in the atmospheric surface layer when compared with the gusty wind disturbances.

atmospheric surface layer, gusty wind disturbances, large-scale motions

PACS number(s): 42.68.Bz, 47.80.Cb, 47.27.wb, 47.27.Jv, 47.27.nb

Citation: H. H. Gu, G. H. Wang, W. Zhu, and X. J. Zheng, Gusty wind disturbances and large-scale turbulent structures in the neutral atmospheric surface layer, Sci. China-Phys. Mech. Astron. **62**, 114711 (2019), https://doi.org/10.1007/s11433-019-9398-5

1 Introduction

The flow motions in the atmospheric surface layer (ASL) are non-uniform and non-stationary, thereby causing an abrupt change in the magnitude of the sporadic wind. This phenomenon, which is often referred to as "gusty wind" by atmospheric scholars [1,2], has attracted an increasing share of attention in atmospheric research [2-6]. The term "gusty wind" was coined by Davenport [1] to refer to the largest instantaneous wind velocities within a given time. This term has also been used in subsequent studies [7,8]. In 1983, the World Meteorological Organization (WMO) clearly defined "gusty wind" as a fluctuation that occurs approximately once every several minutes. However, scholars have described gusty winds on different temporal scales. For example, wind velocities lasting for 3-4 min were defined as "strong gusts" in the field observations presented in ref. [9], whereas the WMO updated their definition of gusty wind as fluctuations lasting for 1-10 min in 2010. Among the various studies that have investigated gusty wind, the temporal scale of this phenomenon is observed to be a controversial issue.

Recently, Zeng and his collaborators [2,10-14] conducted a series of experimental and numerical studies on "gusty wind". Zeng et al. [2] decomposed the three-dimensional atmospheric wind velocities into three parts (the basic mean flow $\overline{u}(t)$ (period>10 min), the gusty wind disturbances $u'_g(t)$ (1 min<period<10 min), and the turbulence fluctuations $u'_t(t)$ (period<1 min). They observed that the gusty wind disturbances are anisotropic with a rather strong co-

*Corresponding author (email: xjzheng@xidian.edu.cn)

herency. The gusty winds are related to very low-frequency internal gravity waves [14]. Cheng et al. [10] simulated turbulent flows in the ASL using the Lagrangian stochastic method. They denoted that the sand/dust particles can be just accumulated (to very low levels) under 1.5 m if the basic mean flow $\overline{u}(t)$ and the turbulent fluctuations $u'_t(t)$ are considered. In the presence of gusty wind disturbances $u'_g(t)$, the sand and dust particles can be entrained into the upper levels of the atmospheric boundary layer; specifically, 37%-43% of the particles can be transported into the 200-m level. In addition, Li et al. [13] statistically analyzed the gusts in the atmospheric boundary layer under weak wind conditions. They reported that the gusty winds contributed approximately 60% of the turbulent kinetic energy (TKE) and 80% of the momentum flux.

Large-scale coherent structures are the typical coherent structures in the ASL. They manifest as very large-scale motions (VLSMs) in high Reynolds number wall-bounded flows [15], which are of considerable importance to the atmospheric research and fluid mechanics communities [16-18]. Recent experimental and numerical investigations have revealed the occurrence of VLSMs in pipe flows [19], channel flows [20], turbulent boundary layer flows [21,22], and ASL flows [23,24]. In the previous decade, ASL studies have revealed streamwise length scales that are 10-15 times the boundary-layer thickness (δ) in the VLSMs of ASL flows with high Reynolds numbers [15]. The VLSMs also contribute significantly to the TKE [24] and significantly influence the small-scale turbulences near the walls [25].

Furthermore, the large-scale turbulent structures play a key role in aeolian sand movements and other natural environments. The aeolian sand movement in natural environments exhibits a complicated intermittent spatiotemporal behavior, such as the presence of aeolian streamers over bare sand surfaces [26,27], and a spatially inhomogeneous dust concentration in the leading edges of the dust storms [2]. Based on the field measurements, Baas [28] reported that long-term scale motions (large-scale motions, LSMs) that are associated with the regional mixing layer play an important role in aeolian sand transport. Zheng et al. [29] observed that the streamwise scales of VLSMs can reach up to 10δ during the stable stage of dust storms, implying the important role played by the VLSMs while transporting dust during the dust storms. The field observations of Wang et al. [30] revealed that the high-speed VLSMs facilitate both the streamwise and upward transportations of PM10 (particles having size of less than 10 μm) in high regions. Further, the turbulent structures in the atmospheric boundary layer also strongly affect the evolution of the wake and the structural response of the wind turbines, as evidenced in both the field measurements and numerical analyses [31,32].

The aforementioned literature denotes that the coherent structures in the ASL, regardless of whether they are termed "gusty wind" or VLSMs/LSMs, are important for TKE and dust transportations; however, the differences between the gusty winds and the VLSMs/LSMs are not thoroughly understood. To discriminate the gusty wind disturbances from large-scale turbulent structures in the ASL and to examine their contributions to the TKE and the momentum flux, we performed real-time synchronous measurements of wind velocities at various heights at the Qingtu Lake Observation Array (QLOA) site (Minqin, China) in 2015.

2 Experimental setup and data preprocessing

The field measurements were conducted at the QLOA site (E: 103°40′03″, N: 39°12′27″). Further, the QLOA can synchronously measure the three-dimensional turbulent ASL flows. The three-component sonic anemometers (Campbell CSAT3B; sampling frequency 50 Hz) were installed on a main tower (at 11 heights ranging from 0.9 to 30 m). For performing the measurements, the anemometers were linked with different acquisition instruments that were synchronized in time using a global positioning system. The details of the experimental facility and QLOA can be observed in the studies conducted by Wang and Zheng [24] and Liu et al. [33]. The turbulent statistics of the neutral ASL data from the QLOA (mean velocity, Reynolds shear stress, and streamwise turbulent intensity) agree well with other experimental and theoretical results in zero-pressure-gradient turbulent boundary layer flows [24].

The QLOA measurements analyzed in this study were acquired from March 24 to June 1, 2015. To ensure statistical convergence, the raw data were split into multiple hourly time series following previous analyses of the ASL data [23,24,34]. The raw velocity data were selected and pretreated as described in the studies conducted by Hutchins et al. [23] and Wang and Zheng [24]. The pretreatments included stratification stability judgment, wind direction adjustment, and steady wind selection. The stability of the ASL was characterized by the Monin-Obukhov stability parameter as follows:

$$\frac{z}{L}=-\frac{\kappa z g\overline{W_s\theta}}{\overline{\theta}u_*^3},$$

where z denotes the measurement height, L denotes the Obukhov length, $\overline{\theta}$ denotes the average temperature at the surface, g denotes the gravitational acceleration, and $\overline{W_s\theta}$ denotes the average vertical heat flux calculated by averaging the covariance between the vertical wind velocity W_s and the temperature θ. The friction velocity u_* can be obtained by fitting the mean streamwise velocity profile [24] or $(-\overline{uw})^{1/2}$ at 2.5 m [23]. Subsequently, the stability criterion in

the current analysis was $z/L<0.06$, implying the presence of a near-neutral boundary layer. The presence of steady wind is an essential condition for analyzing the turbulence statistics. The non-stationary index (IST) was calculated in accordance with the method proposed by Foken et al. [35].

$$IST = \left| (CV_{\mathrm{m}} - CV_{1\,\mathrm{h}}) / CV_{1\,\mathrm{h}} \right| \times 100\%,$$

where $CV_{1\,\mathrm{h}}$ denotes the total streamwise velocity variance per hour and $CV_{\mathrm{m}} = \sum_{i=1}^{12} CV_i / 12$, where CV_i (i=1, 2, ⋯, 12) denotes the local variance of the streamwise velocity in each five-minute period of the hour. The time-series satisfying the high-quality data condition ($IST \leq 20\%$) were selected for performing the analysis.

After data processing, 12 datasets of clean air were selected from the QLOA ($Re_* \approx 2.29\times10^6$ to 4.76×10^6, where $Re_* = u_*\delta/\nu$). Here, the kinematic viscosity ν was calculated from the barometric pressure and temperature at the test site. The ASL thickness (δ=150 m) was estimated as the mean ASL thickness in previous studies at the QLOA observation site [24,33]. Table 1 presents essential information of the neutral ASL data in the present analysis.

3 Temporal scales of the gusty wind disturbances and the VLSMs/LSMs

To clarify that the time scales and energy fractions differ between the gusty wind disturbances and the VLSMS/LSMs, we obtained their normalized energy spectra using the wavelet transform method [28,29,36]. The wavelet transform method and Daubechies bases (db3) decomposes the streamwise velocity time series $u(t)$ as follows:

$$[W_\psi u](b,a) = \frac{1}{|a|^{1/2}} \int_{-\infty}^{+\infty} u(t)\psi\left(\frac{t-b}{a}\right)\mathrm{d}t,\ u \in L^2(R), \tag{1}$$

$$\psi_{b,a}(t) = \frac{1}{|a|^{1/2}}\psi\left(\frac{t-b}{a}\right), \tag{2}$$

where $\psi_{b,a}(t)$ denotes the basis functions of the Daubechies wavelet, and $a = 2^j$ (j = 1, ⋯, p) and b = 1, ⋯, T_n are the dilation and translation factors, respectively. T_n denotes the period of the datasets (T_n=1 hour in this study), and p represents the decomposition order (p=18 in this study). The jth-order sub-scale wind signals $u^j(t)$ are further obtained using the inverse transform.

$$u^j(t) = \frac{1}{C'_\psi |a|^{3/2}} \int_{-\infty}^{\infty} [W_\psi u](b,a)\psi_{b,a}\mathrm{d}b,\ a = 2^j, \tag{3}$$

where $C'_\psi = \pi\int_{-\infty}^{+\infty} \frac{|\widehat{\psi}(\omega)|^2}{|\omega|}\mathrm{d}\omega$, $\widehat{\psi}(\omega) = \int_{-\infty}^{+\infty} \psi_{0,1}(t)\mathrm{e}^{-\mathrm{i}\omega t}\mathrm{d}t$, and ω denotes the circular frequency. The sub-scale wind energy spectra E_u^j and the normalized sub-scale wind energy spectra $S_{\mathrm{nor}}^j(u)$ are respectively calculated as:

$$\begin{aligned} E_u^j &= \sum_{k=1}^{T_n} [u^j(t) - \overline{u}^j]^2 / T_n, \\ \overline{u}^j &= \sum_{k=1}^{T_n} [u^j(t)] / T_n, \\ S_{\mathrm{nor}}^j(u) &= E_u^j / \sigma_u^2. \end{aligned} \tag{4}$$

According to Zeng and his collaborators [2,10-14], the gusty winds (very low-frequency disturbances) occur approximately once every 1-10 min. Therefore, the frequencies (reciprocal periods) of the gusty winds in the normalized energy spectra are 0.0017-0.017 Hz. The decomposition orders of the gusty wind in the wavelet transform are 12-15 (gray area in Figure 1). The VLSMs and LSMs differ from the gusty winds and are generally characterized by their spatial scales. Guala et al. [19] and Balakumar and Adrian [20] investigated the pre-multiplied power spectra of the velocity fluctuations in turbulent pipe flows, channel flows,

Table 1 The main parameters of the selected ASL data (Set. 1-Set. 12)

No.	Time and date	u_*	$Re_*(\times10^6)$	z/L	IST (%)
Set. 1	03 April 03:00-04:00	0.26	2.29	−0.023	18
Set. 2	03 April 02:00-03:00	0.27	2.38	−0.042	13
Set. 3	03 April 01:00-02:00	0.29	2.56	−0.027	15
Set. 4	02 April 21:00-22:00	0.30	2.62	−0.026	11
Set. 5	02 April 20:00-21:00	0.35	3.09	−0.025	10
Set. 6	10 April 18:00-19:00	0.36	3.18	−0.013	8
Set. 7	10 April 17:00-18:00	0.42	3.71	−0.059	9
Set. 8	30 April 00:00-01:00	0.44	3.88	0.013	15
Set. 9	10 May 07:00-08:00	0.46	4.06	−0.051	3
Set. 10	30 April 08:00-09:00	0.48	4.24	−0.027	16
Set. 11	27 May 20:00-21:00	0.50	4.41	0.003	7
Set. 12	30 April 04:00-05:00	0.54	4.76	0.011	6

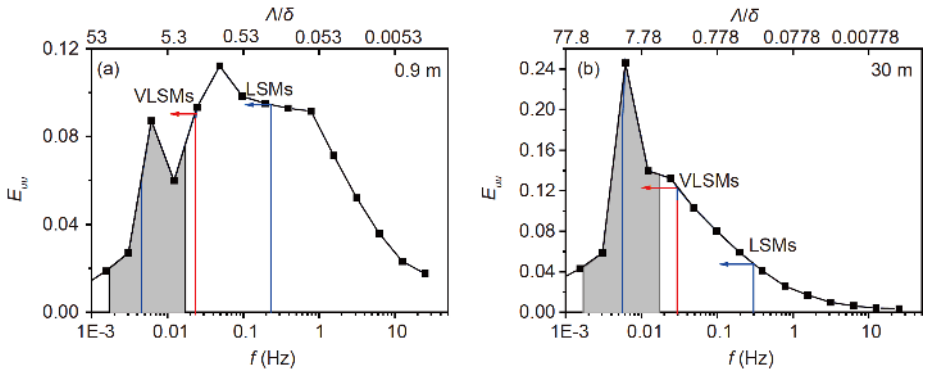

Figure 1 (Color online) The normalized energy spectra of the streamwise wind velocities measured at 0.9 m (a) and 30 m (b) on 08:00-09:00 on April 30, 2015 (No. 10). The upper and lower *x*-axes in each panel represent the frequency and the length scale (normalized by the surface layer thickness δ), respectively.

and boundary layers and determined the criteria for distinguishing between the VLSMs and LSMs. The maximum streamwise extent and the length scales of the LSMs were approximately 3δ and 0.3δ–3δ, respectively. The frequency ranges of the LSMs and VLSMs can be obtained by Taylor's frozen turbulence hypothesis $f = \overline{u} / L$, where $\overline{u}$ denotes the mean velocity and L denotes the cutoff length (0.3δ and 3δ). Taking No.10 as an example, the mean wind velocities at 0.9 and 30 m were $\overline{u}_{0.9\mathrm{m}} = 8.03$ m/s and $\overline{u}_{30\mathrm{m}} = 11.67$ m/s, respectively. Therefore, the frequency ranges of the LSMs and VLSMs at 0.9 m were determined as 0.018-0.18 and 0.0036-0.018 Hz, respectively (see Figure 1(a)). The decomposition orders of the LSMs and VLSMs for No. 10 at z= 0.9 m in the wavelet transform were 8-11 and 12-14, respectively. Similarly, 8-10 and 11-13 for the orders of the LSMs and VLSMs at z=30 m. By considering the difference in the frequency ranges, the decomposition orders in the wavelet transform were 12-15 for the gusty winds and 8-14 (at 0.9 m) and 8-13 (at 30 m) for the LSMs/VLSMs. Note that the VLSMs/LSMs contain 8-11th orders of the sub-scale wind signals in their wavelet transforms, which are absent from the transforms of the gusty winds. Meanwhile, the LSMs/VLSMs lose the information of the 15th-order and the 14-15th-order wind velocity fluctuations at 0.9 and 30 m, respectively, which appear in the gusty winds. However, as depicted in Figure 1, the energy fractions of the 14-15th orders in the wavelet transform are all observed to be lower than 5%.

According to the aforementioned analysis, the decomposition orders in the wavelet transform were 12-15 for the gusty winds and 8-14 for the LSMs/VLSMs (at z=0.9 m during the 08:00-09:00 period on April 30, 2015). The streamwise wind velocity fluctuations of the gusty wind and VLSMs/LSMs determined using the wavelet transform are displayed in Figure 2. The gusty wind fluctuations reflect the large-scale information of the VLSMs/LSMs (Figure 2(a)) but lose the 8-11th order of the sub-scale wind signals (Figure 2(b)), which belong to the LSMs and part of the

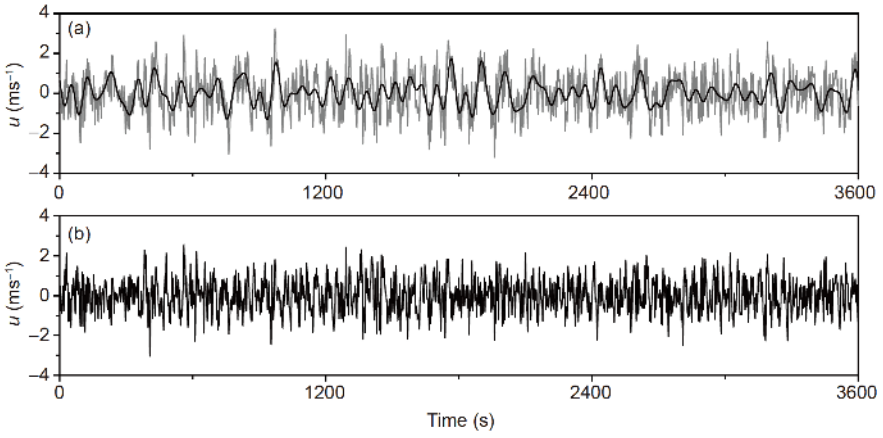

Figure 2 (a) The streamwise wind velocity fluctuations in the gusty wind (black line $\sum_{j=12}^{15} u^j(t)$) and the VLSMs/LSMs (gray line $\sum_{j=8}^{14} u^j(t)$) in the wavelet transform at 0.9 m during the 08:00-09:00 period on April 30, 2015. (b) The additional streamwise wind velocity fluctuations in the wavelet transform $\sum_{j=8}^{11} u^j(t)$.

VLSMs. By considering the significant contributions of VLSMs and LSMS to the TKE and the momentum flux [20], the subsequent section will compare the TKE and momentum flux contributions of the VLSMs/LSMs and gusty winds.

4 Results and discussion

The fluctuations in the VLSMs and LSMs were obtained by low-pass filtering (with a cutoff length of 0.3δ) and band-pass filtering (with cutoff lengths of 0.3δ-3δ) [19,24]. The gusty wind disturbances were obtained by band-pass filtering (with cutoff time scales of 60-600 s) [2,11]. Further, the fractional energy contributions of the VLSMs, LSMs, and gusty wind disturbances (denoted as EF_{VL}, EF_{L}, and EF_{g}, respectively) to the total streamwise TKE are obtained as follows:

$$EF_{VL} = \overline{u'_{VL}u'_{VL}} / \overline{u^2},\ EF_{L} = \overline{u'_{L}u'_{L}} / \overline{u^2},\\ EF_{g} = \overline{u'_{g}u'_{g}} / \overline{u^2}, \tag{5}$$

where u'_{VL}, u'_{L}, and u'_{g} denote the streamwise fluctuations of the VLSMs, LSMs, and gusty wind disturbances, respectively.

Meanwhile, the fractional momentum combinations of the VLSMs, LSMs, and gusty wind disturbances (denoted as MF_{VL}, MF_{L}, and MF_{g}, respectively) to the total momentum flux are determined by

$$MF_{VL} = \overline{u'_{VL}w'_{VL}} / \overline{u'w'},\ MF_{L} = \overline{u'_{L}w'_{L}} / \overline{u'w'},\\ MF_{g} = \overline{u'_{g}w'_{g}} / \overline{u'w'}, \tag{6}$$

where w'_{VL}, w'_{L}, and w'_{g} denote the wall-normal fluctuations of the VLSMs, LSMs, and gusty wind disturbances, respectively.

Figure 3 depicts the height variations of the energy and momentum fractions of the VLSMs, LSMs, and gusty wind disturbances. As depicted in Figure 3(a), EF_{VL}+EF_{L} for all the datasets increased approximately log-linearly with the height and was maximized at approximately 0.93. At all the heights, EF_{g} was considerably less than EF_{VL}+EF_{L}. The MF_{VL}+MF_{L} values also increased log-linearly with height (up to 0.96) and were considerably larger than MF_{g} (Figure 3(b)).

Figure 4 depicts the additional contributions (above the gusty wind disturbances) by the LSMs and part of the VLSMs to the streamwise TKE and momentum flux of the wind fluctuations (denoted as EF_{extra} and MF_{extra}, respectively). As depicted in Figure 4(a), the variations of EF_{extra} increased toward their maximum of 0.53 at z/δ=0.033 and then decreased at higher sites. The MF_{extra} values ranged from 0.2 to 0.67, reaching a maximum at z/δ=0.1 (see Figure 4(b)). Therefore, we can reasonably conclude that the LSMs and part of the VLSMs contribute considerably higher fractions to the streamwise TKE and momentum flux of the wind fluctuations when compared to that contributed by the gusty wind disturbances.

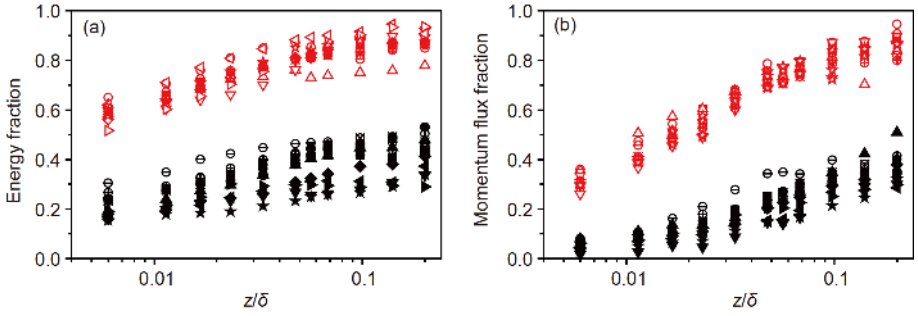

Figure 3 (Color online) The height variations of (a) EF_{VL}+EF_{L} (red symbols) and EF_{g} (black symbols) and (b) MF_{VL}+MF_{L} (red symbols) and MF_{g} (black symbols).

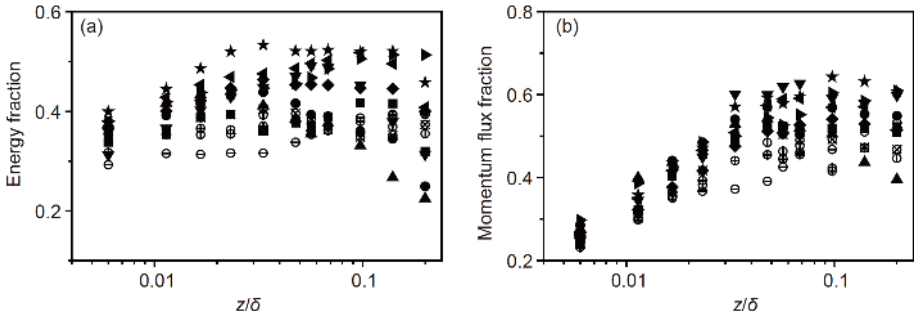

Figure 4 The height variations of (a) EF_{extra} and (b) MF_{extra}.

The temporal scales of the VLSMs and LSMs varied with the wind speed; however, the temporal scale of the gusty wind was invariable during the 60-600-s period. This implies that the variations in the contributions to the streamwise TKE and momentum flux by the LSMs, VLSMs, and gusty wind disturbances may be accompanied by the variations in the frictional wind velocities. As depicted in Figure 4, the differences between the contributions to the streamwise TKE and momentum flux of the VLSMs/LSMs and the gusty wind disturbances were largest at z/δ=0.033 and z/δ=0.1, respectively. Therefore, we plot the EF_{extra} and MF_{extra} variations at z/δ=0.033 and z/δ=0.1 as the functions of friction velocity in Figure 5(a) and (b), respectively. Both EF_{extra} and MF_{extra} increased with the friction velocity, suggesting that the gusty wind disturbances lose more information from the LSMs and VLSMs as the friction velocity increases.

Additionally, turbulent fluctuations with periods of less than 1 min were defined as small-scale turbulences by Zeng and his collaborators [2,10-14]. They suggested that these small-scale turbulences are almost isotropic. However, our results denote that the wind fluctuations with periods of lower than 1 min still contain coherent structures, which are presented in the LSMs and VLSMs. It has been accepted that LSMs and VLSMs are significantly anisotropic and contain a considerable portion of the TKE [20]. Meanwhile, the small-scale turbulences are generally defined as turbulent fluctuations on spatial scales of less than 0.3δ. Therefore, clarifying the difference between the energy contributions from small-scale turbulences as defined by the atmospheric scholars (type-I) and fluid mechanics scholars (type-II) is vital. We denote the TKE components of the TKE contributed by type-I small-scale turbulences as E_u^{I}, E_v^{I}, E_w^{I}, and that contributed by type-II small-scale turbulences as E_u^{II}, E_v^{II}, E_w^{II}. Figure 6 plots E_v^{I}, E_w^{I} versus E_u^{I} and E_v^{II}, E_w^{II} versus E_u^{II} at 30 m in this study. As depicted in Figure 6(a), E_v^{I} and E_w^{I} were smaller than E_u^{I} in most of the cases, indicating that the type-I turbulent fluctuations are significantly anisotropic. Meanwhile, E_u^{II}, E_v^{II}, E_w^{II} were almost equal (Figure 6(b)), implying that the fluctuations on spatial scales of less than 0.3δ are nearly isotropic. Remarkably, we observe that $E_u^{\text{I}} > E_u^{\text{II}}$, $E_v^{\text{I}} > E_v^{\text{II}}$, and $E_w^{\text{I}} > E_w^{\text{II}}$, indicating that the gusty wind can precisely divide all the LSMs and some VLSMs into small-scale turbulences.

5 Conclusions

The differences between the gusty wind disturbances and

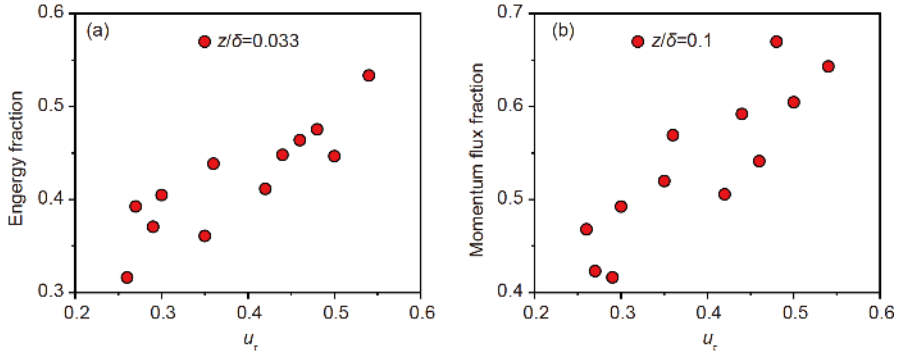

Figure 5 (Color online) The friction velocity variations of EF_{extra} and MF_{extra} at z/δ=0.033 and z/δ=0.1.

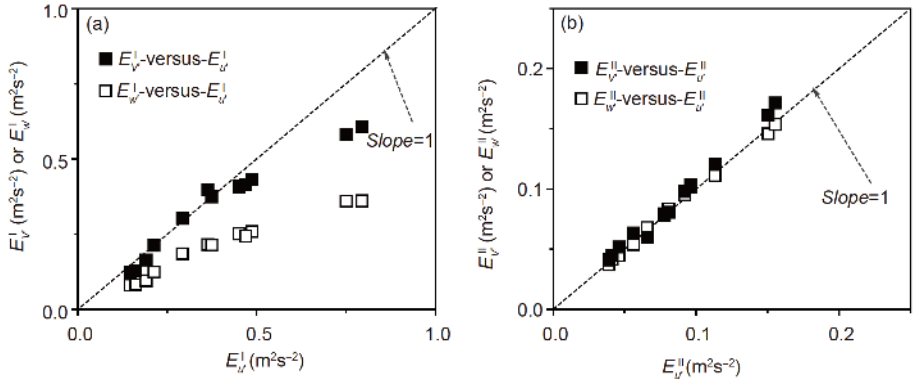

Figure 6 (a) Three components of turbulent kinetic energy E_u^{I}, E_v^{I}, E_w^{I} at 30 m. E_v^{I} versus E_u^{I} (solid symbols) and E_w^{I} versus E_u^{I} (open symbols). (b) Three components of turbulent kinetic energy E_u^{II}, E_v^{II}, E_w^{II} at 30 m: E_v^{II} versus E_u^{II} (solid symbols) and E_w^{II} versus E_u^{II} (open symbols).

VLSMs/LSMs were analyzed using the ASL measurement data obtained from the QLOA site at different wind velocities. The contributions of the VLSMs and LSMs to the streamwise TKE and momentum flux were more important than the contributions of the gusty wind disturbances. Specifically, the gusty wind disturbances and VLSMs/LSMs contributed approximately 0.2-0.53 and 0.52-0.93 in the streamwise TKE, respectively, and up to 0.53 and 0.90 in the momentum flux, respectively. The large-scale coherent structures in the gusty wind disturbances contained a certain portion of the streamwise TKE and momentum flux of the wind fluctuations. These contributions increased with the friction velocity, reaching maximum values of 0.53 and 0.67, respectively. The VLSMs and LSMs contribute more to the TKE and the momentum flux of the wind fluctuations when compared to the contributions of the gusty wind disturbances. Therefore, the VLSMs/LSMs can better describe the flow characteristics and coherent structures in the ASL.

It should be noted that different scholars have expressed various opinions about the period of gusty wind. In this study, the gusty disturbances were considered to appear once per 1-10 min, which was consistent with the observation of Zeng and his collaborators. The present field experiment was conducted in a desert area, and our results (that the VLSMs/LSMs can well describe the flow characteristics and coherent structures in the ASL) provide experimental evidence for aeolian sand transport in further research. However, the differences between the gusty wind disturbances and the VLSMs/LSMS under other flow conditions require further research.

This work was supported by the National Natural Science Foundation of China (Grant Nos. 11490553, and 11702122), and the Fundamental Research Funds for the Central Universities (Grant No. lzujbky-2017-30).

1 A. G Davenport, Proc Inst Civ Eng. **28**, 187 (1964).
2 Q. Zeng, X. Cheng, F. Hu, and Z. Peng, Adv. Atmos. Sci. **27**, 1 (2010).
3 S. Barth, F. Böttcher, and J. Peinke, Proc. Appl. Math. Mech. **5**, 561 (2010).
4 O. Brasseur, Mon. Wea. Rev. **129**, 5 (2001).
5 S. Goyette, O. Brasseur, and M. Beniston, J. Geophys. Res. **108**, 4374 (2003).
6 R. H. Sherlock, J. Aeron. Sci. **5**, 53 (1937).
7 M. E. Greenway, J. Wind Eng. Indust. Aerodyn. **5**, 61 (1979).
8 C. J. Wood, J. Wind Eng. Indust. Aerodyn. **12**, 385 (1983).
9 Z. PetkovSek, Geofizika **4**, 41 (1987).
10 X. L. Cheng, Q. C. Zeng, and F. Hu, Chin. Sci. Bull. **57**, 3595 (2012).
11 X. Cheng, L. Wu, F. Hu, and Q. C. Zeng, J. Geophys. Res. **117**, D08113 (2012).
12 L. Wu, X. Cheng, Q. Zeng, J. Jin, J. Huang, and Y. Feng, J. Geophys. Res. Atmos. **122**, 5976 (2017).
13 Q. L. Li, X. L. Cheng, and Q. C. Zeng, Atmos. Ocean. Sci. Lett. **9**, 52 (2016).
14 X. L. Cheng, Q. C. Zeng, F. Hu, and Z. Peng, Clim. Environ. Res. **12**, 227 (2007).
15 N. Hutchins, and I. Marusic, Philos. Trans. R. Soc. A-Math. Phys. Eng. Sci. **365**, 647 (2007).
16 J. C. R. Hunt, and J. F. Morrison, Eur. J. Mech.-B/Fluids **19**, 673 (2000).
17 A. J. Smits, B. J. McKeon, and I. Marusic, Annu. Rev. Fluid Mech. **43**, 353 (2011).
18 M. Horiguchi, T. Hayashi, A. Adachi, and S. Onogi, Bound.-Layer Meteorol **144**, 179 (2012).
19 M. Guala, S. E. Hommema, and R. J. Adrian, J. Fluid Mech. **554**, 521 (2006).
20 B. J. Balakumar, and R. J. Adrian, Philos. Trans. R. Soc. A-Math. Phys. Eng. Sci. **365**, 665 (2007).
21 J. H. Lee, and H. J. Sung, J. Fluid Mech. **673**, 80 (2011).
22 M. Vallikivi, B. Ganapathisubramani, and A. J. Smits, J. Fluid Mech. **771**, 303 (2015).
23 N. Hutchins, K. Chauhan, I. Marusic, J. Monty, and J. Klewicki, Bound.-Layer Meteorol **145**, 273 (2012).
24 G. Wang, and X. Zheng, J. Fluid Mech. **802**, 464 (2016).
25 R. Mathis, N. Hutchins, and I. Marusic, J. Fluid Mech. **628**, 311 (2009).
26 A. C. W. Baas, and D. J. Sherman, J. Geophys. Res. **110**, F03011 (2005).
27 A. C. W. Baas, Geomorphology **93**, 3 (2008).
28 A. C. W. Baas, Geophys. Res. Lett. **33**, L05403 (2006).
29 X. J. Zheng, J. H. Zhang, G. H. Wang, H. Y. Liu, and W. Zhu, Sci. China-Phys. Mech. Astron. **56**, 306 (2013).
30 G. H. Wang, X. J. Zheng, and J. J. Tao, Phys. Fluids. **29**, 1 (2017).
31 D. S. Li, T. Guo, Y. R. Li, J. S. Hu, Z. Zheng, Y. Li, Y. J. Di, W. R. Hu, and R. N. Li, Sci. China-Phys. Mech. Astron. **61**, 94711 (2018).
32 Z. Zheng, Z. T. Gao, D. S. Li, R. N. Li, Y. Li, Q. H. Hu, and W. R. Hu, Sci. China-Phys. Mech. Astron. **61**, 94712 (2018).
33 H. Y. Liu, T. L. Bo, and Y. R. Liang, Phys. Fluids **29**, 035104 (2017).
34 J. C. Wyngaard, Q. J. Roy Meteor. Soc. **24,** 316 (1992).
35 T. Foken, M. Goockede, M. Mauder, L. Mahrt, B. Amiro, and W. Munger, in *Handbook of Micrometeorology* (Springer, Netherlands, 2004), p. 181.
36 M. Farge, Annu. Rev. Fluid Mech. **24**, 395 (1992).